NANO LETTERS

pubs.acs.org/NanoLett Letter

# Spontaneous Curvature Sculpts Filament–Vesicle Morphogenesis

Yaxin Fang, Chengyao Zhang, Meng Wang, Chao Shi, and Xin Yi*

Cite This: *Nano Lett.* 2026, 26, 10273–10280 Read Online

ACCESS | Metrics & More | Article Recommendations | Supporting Information

**ABSTRACT:** Membrane-bound filaments are central to cellular morphogenesis, yet how spontaneous curvature regulates filament–membrane coupling under geometric confinement remains unclear. Here we show that spontaneous curvature fundamentally reorganizes filament–membrane morphogenesis in vesicles by biasing the competition between membrane deformation and filament bending. Using a unified curvature-elasticity framework that couples membrane and filament curvature energetics, we construct phase diagrams for vesicles enclosing filament loops and demonstrate that spontaneous curvature selects distinct symmetry-breaking pathways, leading to both continuous and discontinuous morphological transitions. In the rigid-filament limit, we further identify an intrinsic accommodation limit imposed by membrane elasticity together with area and volume conservation, beyond which no mechanically equilibrated configuration exists. These findings establish spontaneous curvature as a powerful design parameter for programming filament–membrane morphogenesis in biological and synthetic systems.

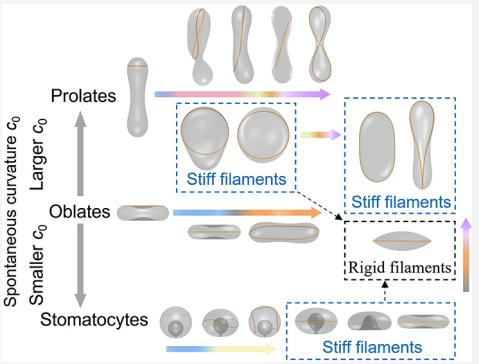


**KEYWORDS:** *filament–vesicle coupling, spontaneous curvature, vesicle confinement, curvature elasticity, symmetry breaking, artificial cells*

Lipid vesicles provide an ideal model system for studying how geometry and curvature elasticity govern shape transformations in soft matter and biological systems, with direct relevance to cellular processes such as endocytosis, organelle shaping, and synthetic-cell design.[1] Vesicle morphogenesis is primarily controlled by membrane spontaneous curvature, which biases local bending, and geometric confinement, commonly quantified by the reduced volume under fixed area and volume constraints.[2] Spontaneous curvature arises from lipid compositional asymmetry, protein adsorption, or leaflet imbalance and drives preferred curvature states.[3,4] Geometric confinement restricts admissible shapes and gives rise to canonical morphologies, including spherical, prolate, oblate, and stomatocyte-like shapes.[5] Together, these effects govern a broad spectrum of membrane remodeling processes, from endocytosis, cargo wrapping, and budding of lipid droplets[5−12] to global shape transformations of cells and vesicles[1,13,14] and membrane adaptation to extreme biological environments.[15] The interplay between spontaneous curvature and geometric confinement becomes substantially richer in the presence of internal filamentous structures.

In living cells and synthetic analogues, vesicles rarely exist as empty containers but instead encapsulate cytoskeletal filaments such as actin filaments and microtubules.[16,17] In bottom-up synthetic-cell platforms, programmable cytoskeletal assemblies have been engineered to organize intracellular contents and mechanically reprogram compartment morphology,[18] while reconstituted systems demonstrate that confinement can direct cytoskeletal organization.[19,20] Vesicles containing confined filaments therefore provide a minimal model for filament–membrane coupling and exhibit a broad spectrum of morphologies.[21−28] Depending on filament length, stiffness, and topology, open filaments generate cherry-, dumpling-, pebble-, and racket-like vesicle shapes,[22,26,29] whereas closed loops yield planar and saddle-shaped filament configurations.[23,26,28] Theoretical and numerical studies have further revealed filament buckling, vesicle stretching, and convex-to-concave transitions in filament–vesicle systems.[30,31] Despite this progress, most studies have focused on elastic or active filaments confined by rigid boundaries[32−34] or deformable vesicles interacting with effectively rigid fibers.[35] However, how spontaneous curvature regulates filament–membrane morphogenesis through the coupled effects of filament elasticity, membrane deformability, and geometric confinement remains largely unexplored.

Here we present a theoretical investigation of a vesicle enclosing a closed filament loop, using a unified curvature-elasticity framework in which membrane bending follows the Helfrich description[36] and filament mechanics is governed by the curvature of its centerline.[37] We show that spontaneous curvature fundamentally reorganizes filament–membrane morphogenesis under geometric confinement. Closed filament loops are considered because topological closure imposes a

**Received:** May 4, 2026
**Revised:** June 30, 2026
**Accepted:** July 10, 2026
**Published:** July 23, 2026

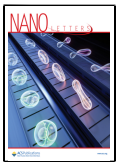





https://doi.org/10.1021/acs.nanolett.6c02160
*Nano Lett.* 2026, 26, 10273−10280

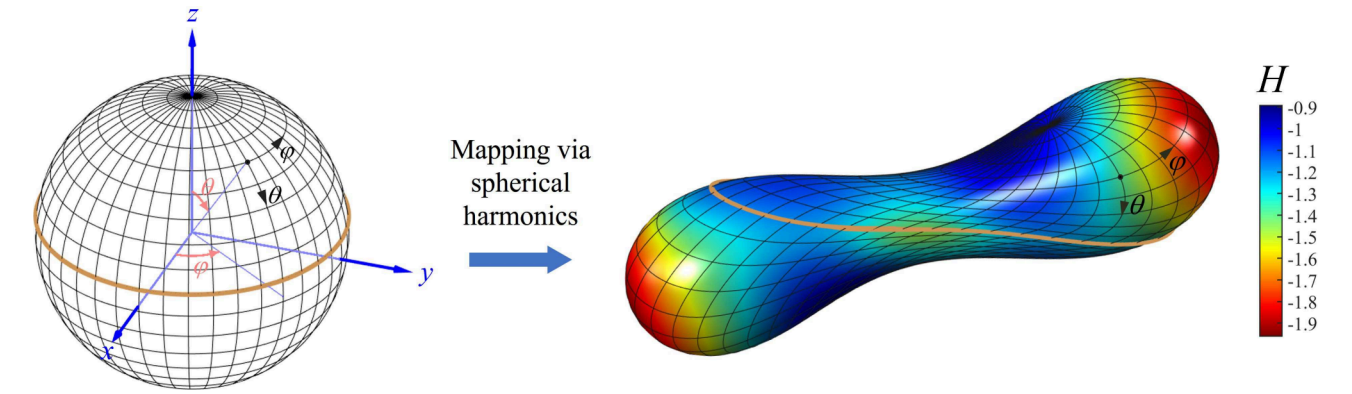


**Figure 1.** Schematic of the filament–vesicle system. A closed, inextensible filament loop (yellow) of length $L$ is constrained on the inner surface of a vesicle with fixed area $A$ and volume $V$. The vesicle surface is parametrized using spherical coordinates $(\theta, \varphi)$, mapping a reference sphere to the deformed shape. The local mean curvature of the membrane is denoted by $H$, which is negative for a spherical vesicle.

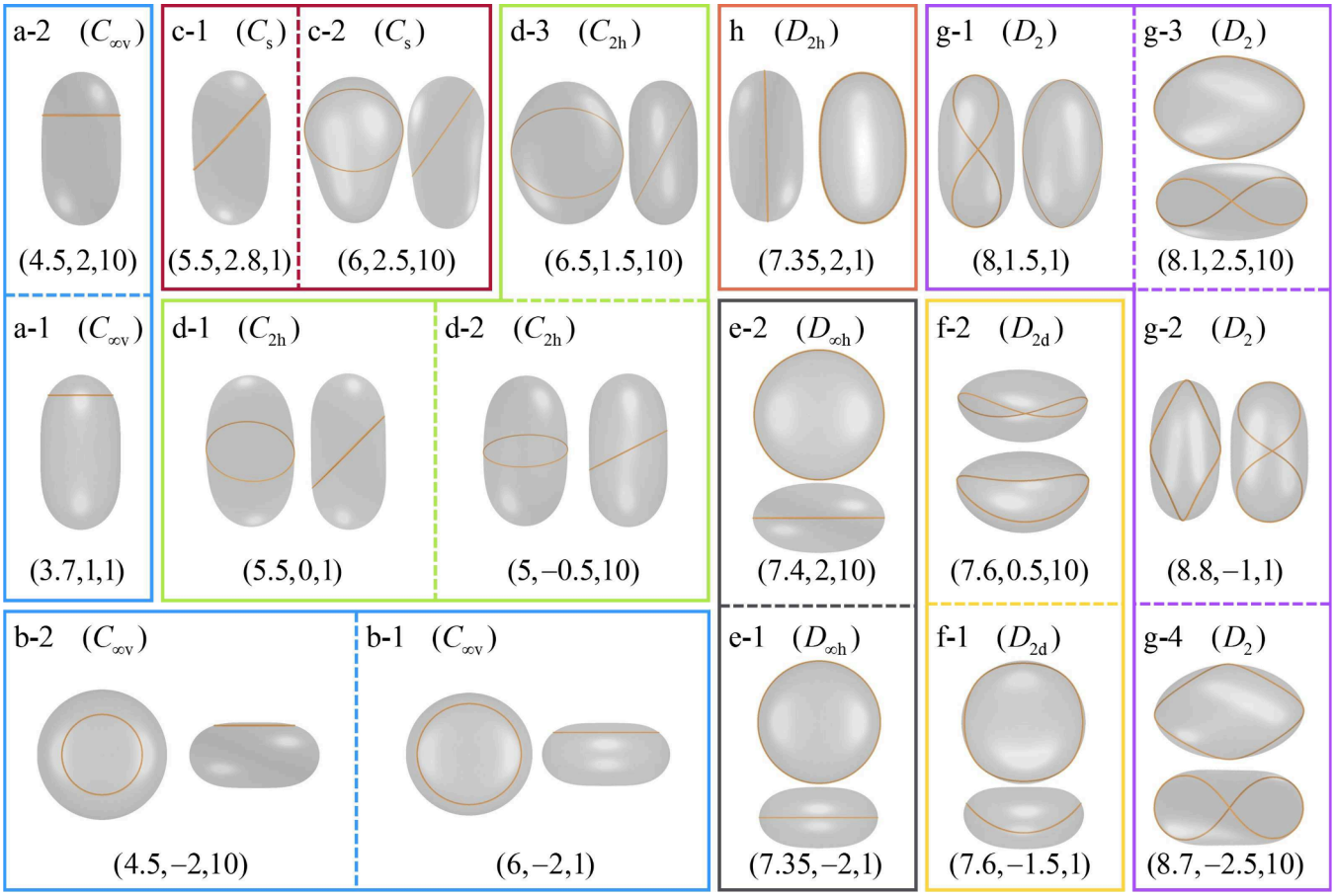


**Figure 2.** Morphologies of the filament–vesicle system at $v = 0.9$ for selected sets $(L/R, c_0R, D/(\kappa R))$. Parameter values are indicated below each configuration. For clarity, selected configurations are shown from multiple viewing angles. Seven distinct symmetry classes are identified, with their corresponding point-group labels indicated in parentheses.

nonlocal geometric constraint, enabling collective buckling and symmetry-breaking modes that are absent in boundary-dominated open filaments. Such looped configurations also capture the networked, quasi-closed organization of cytoskeletal filaments in cells. We map morphological phase behavior across filament length, stiffness, spontaneous curvature, and reduced volume. We show that spontaneous curvature selectively shifts the dominant elastic mode between membrane bending and filament deformation, thereby controlling the instability mechanisms that govern symmetry breaking. This curvature-dependent redistribution of elastic energy leads to distinct transition pathways and gives rise to both continuous and discontinuous morphological transitions. In the rigid-filament limit, we further identify an intrinsic accommodation threshold beyond which mechanically equilibrated configurations cease to exist.

Consider a filament–vesicle system (Figure 1) consisting of a closed, inextensible filament of total length $L$ constrained to the inner surface of a lipid vesicle of fixed area $A(= 4\pi R^2)$ and volume $V$, where $R$ is the effective vesicle radius. The filament


https://doi.org/10.1021/acs.nanolett.6c02160
Nano Lett. 2026, 26, 10273–10280

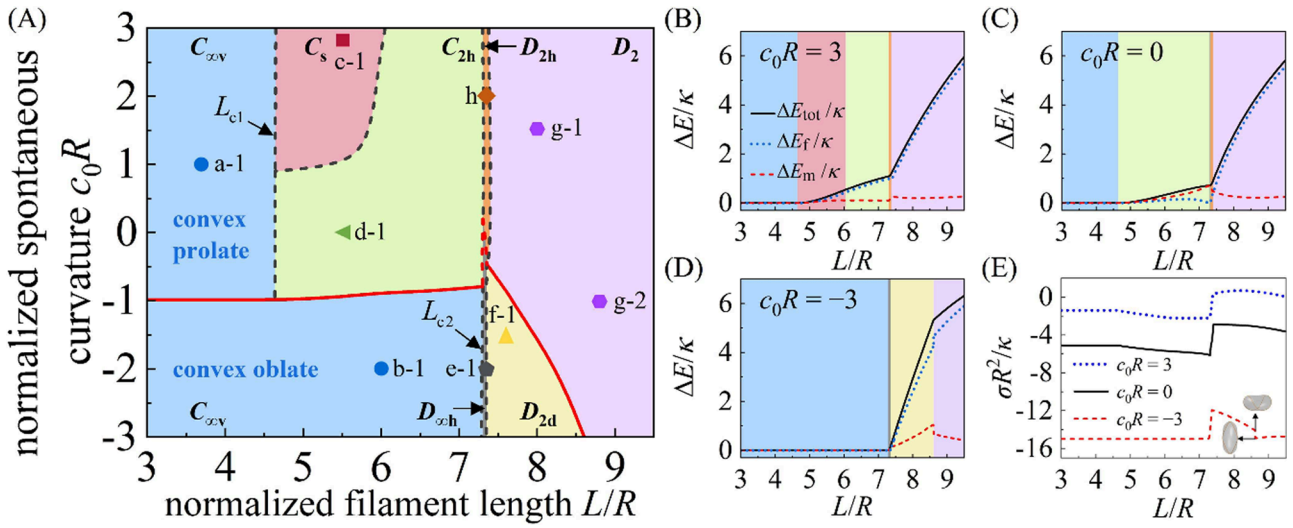


**Figure 3.** Curvature-dependent instability and phase behavior of the filament−vesicle system at $v = 0.9$ and $D/(\kappa R) = 1$. (A) Morphological phase diagram in $L/R$−$c_0R$ space, with symbols corresponding to the morphologies in Figure 2. Dashed and solid boundaries denote continuous and discontinuous transitions, respectively; the red boundary separates prolate- and oblate-derived vesicle states. (B−D) Profiles of the total energy change $\Delta E_{tot}$ and its components $\Delta E_f$ and $\Delta E_m$ at $c_0R = 3$, 0, and −3, respectively. (E) Profiles of the normalized membrane tension $\sigma R^2/\kappa$ for $c_0R = -3$, 0, and 3. Insets show representative configurations across the discontinuous transition. An enlarged view of the tension discontinuity and the corresponding energy profiles are provided in Figures S3 and S4. Positive (negative) $\sigma$ corresponds to tensile (compressive) membrane tension.

is modeled as a homogeneous wormlike chain with bending stiffness $D$. The vesicle membrane is characterized by bending rigidity $\kappa$ and spontaneous curvature $c_0$. The total system energy $E_{tot}$, comprising the filament bending energy $E_f$ and the membrane bending energy $E_m$, is given by[36,37]

$$E_{tot} = E_f + E_m, \quad E_f = \frac{D}{2}\int_0^L C^2 ds, \quad E_m = \frac{\kappa}{2}\int (2H + c_0)^2 dA$$

where $C$ and $ds$ represent the local curvature and arclength element of the filament, respectively, while $H$ and $dA$ denote the mean curvature and surface element of the vesicle membrane, respectively. Here, $H = -1/R$ for a spherical vesicle of radius $R$ under the present sign convention. A positive $c_0$ favors outward bending, whereas a negative $c_0$ favors inward bending toward the vesicle interior. No torsional degree of freedom is included in the filament model.

Rescaling energies by $\kappa$ and lengths by $R$, the equilibrium configuration is governed by four dimensionless parameters: the stiffness ratio $D/(\kappa R)$, the normalized filament length $L/R$, the normalized spontaneous curvature $c_0R$, and the reduced volume $v = 3V/(4\pi R^3)$. Fixing both membrane area and enclosed volume generally produces nonspherical vesicle shapes, thereby generating intrinsically anisotropic soft confinement for the filament. This confinement couples filament bending and reorientation to membrane deformation and underlies the morphology selection analyzed below.

To determine equilibrium configurations, we represent the vesicle shape using a spherical-harmonic parametrization[38] and obtain stationary states via constrained minimization[39] of $E_{tot}$. Details of the parametrization and constrained minimization are provided in Note 1 of the Supporting Information (SI).

Before introducing the filament, we consider filament-free vesicles as reference states (Figure S1). We focus on two representative reduced volumes, $v = 0.9$ and 0.65, which define distinct confinement landscapes for the enclosed filament. At $v = 0.9$, the vesicle remains convex, whereas at $v = 0.65$, reduced volume induces concavity and necked confinement. These contrasting geometries provide complementary settings for probing filament-induced morphology selection.

The presence of filaments can significantly influence vesicle morphologies. To elucidate how filament−vesicle coupling governs morphology selection, we systematically vary the spontaneous curvature $c_0R$ and the relative filament stiffness $D/(\kappa R) = 1$, 10, and $\infty$ across $v = 0.9$ and 0.65.

We first consider convex confinement at $v = 0.9$. Representative equilibrium configurations for selected values of normalized filament length $L/R$ and spontaneous curvature $c_0R$, at $D/(\kappa R) = 1$ and 10, are shown in Figure 2. These configurations, classified using Schönflies point-group notation (Table S1), span seven symmetry classes. The corresponding morphological phase diagrams are given in Figure 3A for $D/(\kappa R) = 1$ and Figure S2A for $D/(\kappa R) = 10$. In the phase diagrams, dashed and solid boundaries denote continuous and discontinuous transitions, respectively, while the red boundary curves separate vesicle states with predominantly prolate-like and oblate-like geometric characters. These states retain the overall features of prolate or oblate vesicle shapes but allow filament-induced deviations.

For a filament-free vesicle (Figure S1A) at $v = 0.9$, the equilibrium shape is an axisymmetric convex prolate for $c_0R > -0.984$, with a maximum radial distance of $0.738R$ from the axis of revolution, and an axisymmetric convex oblate for $c_0R < -0.984$, with a maximum radial distance of $1.162R$. In both cases, these characteristic radial distances are insensitive to $c_0R$, defining two thresholds for the coupled system. Accordingly, when $L \le L_{c1} = 2\pi \times 0.738R = 4.637R$ in the prolate vesicle state (e.g., Figure 2a-1,a-2), or $L \le L_{c2} = 2\pi \times 1.162R = 7.30R$ (e.g., Figure 2b-1,b-2) in the oblate vesicle state, the filament remains circular regardless of stiffness, and the system retains axisymmetric $C_{\infty v}$ symmetry (blue regions in Figures 3A and S2A). For $L > L_{c1}$ or $L > L_{c2}$, confinement-induced compression destabilizes the circular configuration, leading to filament reorientation and buckling and, consequently, successive symmetry breaking.



https://doi.org/10.1021/acs.nanolett.6c02160
Nano Lett. 2026, 26, 10273−10280

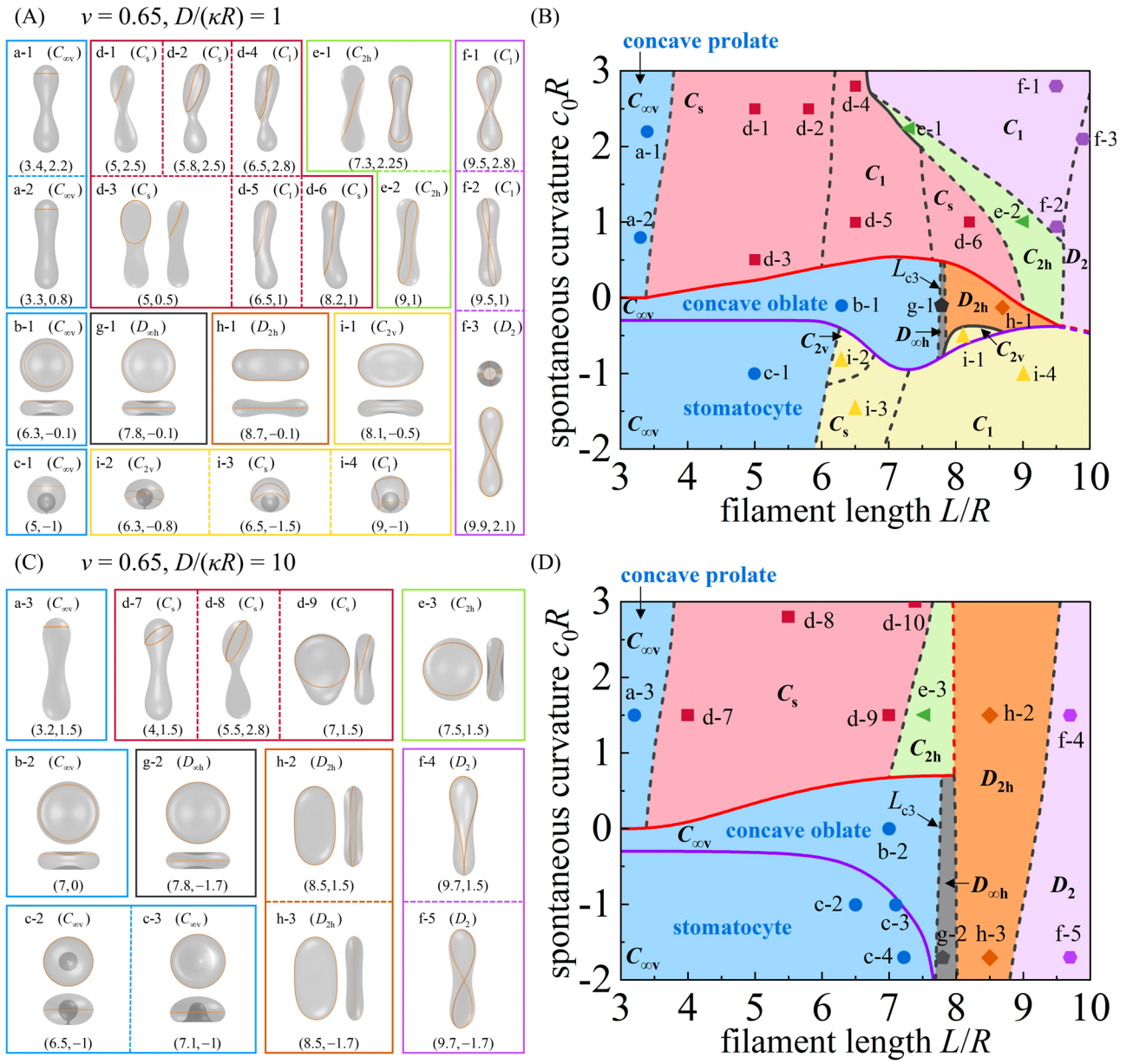


**Figure 4.** Morphologies and phase behavior of the filament−vesicle system at $v = 0.65$. (A,B) Flexible filaments, $D/(\kappa R) = 1$. (A) Representative configurations for selected $(L/R, c_0R)$; some configurations are shown from multiple viewing angles. Eight distinct symmetry classes are identified (labels in parentheses). (B) Corresponding phase diagram; symbols correspond to the representative configurations in (A). The threshold $L_{c3}$ decreases slightly with decreasing $c_0R$, from $L_{c3}/R = 7.776$ at $c_0R = 0.485$ to 7.734 at $c_0R = -0.8$. (C,D) Stiff filaments, $D/(\kappa R) = 10$. (C) Representative configurations for selected $(L/R, c_0R)$, showing six symmetry classes (labels in parentheses). (D) Corresponding phase diagram; symbols map to the configurations in (C). Configurations labeled c-4 and d-10 in (D) are shown in Figure S6. Here, $L_{c3}/R$ decreases from 7.76 at $c_0R = 0.7$ to 7.71 at $c_0R = -2$. In (B) and (D), dashed and solid lines indicate continuous and discontinuous morphological transitions, respectively. Red and purple boundaries separate prolate−oblate and oblate−stomatocyte vesicle states.

In the prolate regime, the post-threshold evolution depends strongly on $c_0R$. For relatively small $|c_0R|$, once $L > L_{c1}$, confinement compresses the filament and drives symmetry breaking. Flexible filaments $(D/(\kappa R) = 1)$ deform readily, allowing the vesicle to remain prolate while the filament reorients into a nearly planar, oval-like configuration (e.g., Figure 2d-1). Stiff filaments $(D/(\kappa R) = 10)$ resist compression more strongly, maintaining a prolate vesicle at smaller $L$ (e.g., Figure 2d-2) but inducing pronounced lateral distortion and eventually driving a transition to an oblate vesicle at larger $L$ (e.g., Figure 2d-3). These $C_{2h}$ configurations correspond to the green regions in Figures 3A and S2A. For sufficiently large positive $c_0R$, the vesicle becomes asymmetric, with one end expanding while the other contracts. The filament remains planar but relocates toward the more spacious end, yielding $C_s$ system configurations that retain a single mirror plane while losing centrosymmetry (e.g., Figure 2c-1,c-2).

In the oblate regime, when $L > L_{c2}$, the equatorial filament loop first expands radially under membrane compression while the coupled system remains axisymmetric with inversion symmetry (e.g., Figure 2e-1; $D_{\infty h}$). Flexible filaments sustain only limited radial expansion before buckling, whereas stiffer filaments slightly enlarge the $D_{\infty h}$ regime by more effectively resisting compression. With further increases in $L$, out-of-plane


https://doi.org/10.1021/acs.nanolett.6c02160
Nano Lett. 2026, 26, 10273−10280

bending becomes favorable, and the filament loop evolves into a saddle-like configuration, leading to $D_{2d}$ system symmetry (Figure 2f-1), followed at larger $L$ by apparently twisted, figure-eight-like states ($D_2$ system symmetry) (Figure 2g-2). Here, "twisted" refers only to the visual appearance of the filament configuration in certain viewing projections (Figure 2g-1 to 2g-4), rather than elastic torsion of the filament cross-section. Increased filament stiffness favors straighter segments, thereby promoting the $D_{2d}$-to-$D_2$ transition to reduce bending in the two half-loops (Figure 2f-2,g-4).

At large positive $c_0R$, further elongation leads to distinct large-$L$ pathways depending on filament stiffness. For flexible filament loops, the oval loops narrow further and align within a plane, yielding $D_{2h}$ symmetry (Figure 2h). A further increase in $L$ triggers a supercritical symmetry-breaking instability that breaks reflection symmetry and drives a $D_{2h}$-to-$D_2$ transition (Figure 2g-1). This transition is identified as supercritical because the filament configuration evolves continuously from a planar oval loop to a spatial out-of-plane buckled state, with the out-of-plane deformation amplitude growing smoothly from zero and without a discontinuous jump in morphology or coexistence of metastable configurations, distinguishing this transition from first-order or subcritical instabilities.

In contrast, stiff filaments resist compression from the confining vesicle, leading instead to vesicle flattening while preserving vertical symmetry and maintaining a $D_{\infty h}$ symmetry (Figure 2e-2). Further increases in $L$ lead to $D_{2d}$ and $D_2$ symmetry (Figure 2g-3).

The phase behavior is governed by a curvature-dependent redistribution of elastic energy between membrane bending and filament deformation. Comparing the phase diagrams for flexible and stiff filaments (Figures 3A and S2A) reveals that filament stiffness primarily restricts configurations involving strong filament narrowing, eliminating the $D_{2h}$ region in the stiff-filament case.

To elucidate this mechanism, we analyze the energy decomposition for flexible filaments ($D/(\kappa R) = 1$) in Figure 3B–D, where $\Delta E_{tot} = \Delta E_m + \Delta E_f$ is measured relative to a filament-free vesicle at $v = 0.9$ with varying $c_0$ and a circular filament of length $L$. Accordingly, the membrane energy change is $\Delta E_m = E_m - E_{m0}$ and the filament bending energy change is $\Delta E_f = E_f - 2\pi^2 D/L$, where $E_{m0} = 7.25\kappa$, $29.90\kappa$, and $164.18\kappa$ at $c_0R = 3$, 0, and −3, respectively.

For $c_0R = 3$ and 0, the system maintains its unperturbed ground state ($\Delta E_{tot} = 0$) for $L \le L_{c1}$, whereas for $c_0R = -3$, the corresponding threshold is $L_{c2} = 7.30R$. Beyond these thresholds, spontaneous curvature determines which elastic contribution dominates the deformation. At high positive curvature ($c_0R = 3$, Figure 3B), $\Delta E_f$ dominates throughout. At $c_0R = 0$, $\Delta E_m$ dominates at intermediate $L/R$, whereas $\Delta E_f$ regains dominance at large $L/R$ (Figure 3C). In contrast, at $c_0R = -3$, deformation beyond $L_{c2}$ is again primarily governed by $\Delta E_f$ (Figure 3D). A parallel energetic analysis for stiff filaments is presented in Figure S2B–D.

This curvature-dependent redistribution of elastic energy directly determines the instability modes that drive symmetry breaking and thus shapes the phase diagram in Figure 3A. Regions dominated by membrane bending favor gradual shape adaptation and continuous transitions, whereas filament-dominated regimes promote buckling-driven instabilities and are more likely to exhibit symmetry breaking.

The corresponding membrane-tension profiles in Figure 3E ($v = 0.9$ and $D/(\kappa R) = 1$) provide independent signatures of these transitions. The membrane tension, $\sigma(= -\partial E_{tot}/\partial A)$, is defined as a Lagrange multiplier conjugated to the fixed vesicle area $A$. For $c_0R = 3$ and 0, the sharp increase in $\sigma$ marks continuous morphological transitions from $C_{2h}$ to $D_{2h}$ symmetry during vesicle flattening. For $c_0R = -3$, the initial sharp rise corresponds to a continuous $C_{\infty v}$-to-$D_{\infty h}$ transition, indicating membrane stretching as the equatorial filament loop expands radially. The subsequent abrupt drop in $\sigma$ signifies a discontinuous $D_{2d}$-to-$D_2$ transition. The energy profiles underlying this discontinuous transition are shown in Figure S4, where the equilibrium boundary is determined by the crossing of two locally stable solution families. The overlap of locally stable solution families suggests possible path dependence under parameter sweeps.

For stiff filaments ($D/(\kappa R) = 10$), $\sigma$ shows a consistently sharp but continuous increase for $c_0R = -3$, 0, and 3 (Figure S5). This behavior accompanies continuous transitions to $D_{\infty h}$ symmetry (from $C_{2h}$ for $c_0R \ge 0$ and $C_{\infty v}$ for $c_0R = -3$), illustrating that increased filament stiffness amplifies the membrane's tensile response during deformation.

Having established the filament–vesicle coupling mechanisms in the convex regime, we now turn to the more complex confinement landscape at $v = 0.65$, where reduced volume introduces pronounced concavity. The corresponding filament-free reference states (Figure S1B) exhibit three stable shapes separated by two critical spontaneous curvatures ($c_0R = 0.006$ and −0.3): concave prolate (dumbbell), concave oblate (discocyte), and stomatocyte shapes. Notably, the emergence of the noncentrosymmetric stomatocyte ($C_{\infty v}$) contrasts with the centrosymmetric ($D_{\infty h}$) shapes at $v = 0.9$, introducing lobe-selective confinement and a constricted neck. This geometric complexity provides a distinct confinement landscape for filament-induced morphogenesis.

These features lead to a substantially richer set of morphologies, as summarized in Figure 4 for flexible ($D/(\kappa R) = 1$) and stiff ($D/(\kappa R) = 10$) filaments. Eight symmetry classes are identified for flexible filaments, compared to six for stiff filaments, reflecting the additional deformation modes enabled by filament flexibility.

For $c_0R > 0.006$, the filament-free vesicle adopts an axisymmetric concave prolate shape with two enlarged end lobes. The corresponding maximum radial distance increases monotonically from $0.538R$ at $c_0R = 0.006$ to $0.604R$ at $c_0R = 3$, setting a curvature-dependent geometric threshold. Filament loops with radii below this scale remain circular, and the system retains axisymmetric $C_{\infty v}$ symmetry (Figure 4a-1 to 4a-3).

Beyond this threshold, two distinct deformation pathways emerge. At intermediate lengths, the filament remains confined within a single lobe, where confinement-induced compression drives reorientation and out-of-plane bending, producing $C_s$ system configurations (Figure 4d-1 to 4d-3, 4d-7, and 4d-8), accompanied by lobe expansion. At larger $L$, the filament overcomes single-lobe confinement and penetrates the constricted neck, extending into the waist region and, in some cases, into the opposing lobe (Figure 4d-9 and Figure S6A for 4d-10). This transition introduces stronger geometric constraints and leads to lower-symmetry configurations, including $C_1$, $C_s$, $C_{2h}$, and $D_2$ states. The apparent twisting of these configurations further depends on the relative alignment between the filament and vesicle axes, with aligned axes observed in Figure 4f-3 and misaligned axes in Figure 4f-1 and 4f-2.



https://doi.org/10.1021/acs.nanolett.6c02160
Nano Lett. 2026, 26, 10273−10280

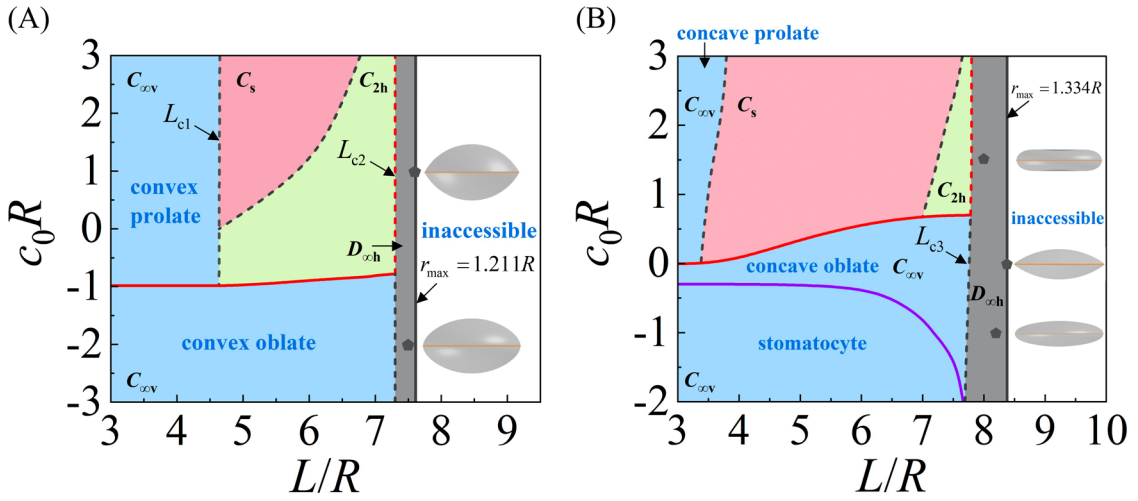


**Figure 5.** Morphological phase diagrams of the rigid filament−vesicle system at $v = 0.9$ (A) and 0.65 (B). Insets show representative equilibrium configurations marked by the pentagon symbols. Dashed and solid lines denote continuous and discontinuous morphological transitions, respectively. For $v = 0.9$, the critical filament lengths are $L_{c1} = 4.637R$ and $L_{c2} = 7.30R$, with an upper bound $L_{max} = 7.609R$. For $v = 0.65$, the critical filament length $L_{c3}$ decreases slightly with decreasing $c_0R$, from $L_{c3}/R = 7.8$ at $c_0R = 3$ to 7.69 at $c_0R = -2$, and an upper bound $L_{max} = 8.382R$.

These observations indicate that, in contrast to the convex case, filament morphogenesis at $v = 0.65$ is governed not only by confinement-induced compression but also by the ability of the filament to overcome neck constraints and explore multilobe configurations.

In the range $-0.3 < c_0R < 0.006$, the filament-free vesicle adopts an axisymmetric concave oblate shape, with a maximum radial distance of approximately $1.234R$. Filament loops shorter than the critical scale $L_{c3} \approx 2\pi \times 1.234R = 7.753R$ remain circular, yielding axisymmetric $C_{\infty v}$ configurations. This threshold $L_{c3}$ exhibits weak dependence on filament stiffness (Figures 4B,4D, and 5B).

For $L > L_{c3}$, the system first undergoes a radially symmetric expansion of the filament loop, accompanied by vesicle flattening and retaining $D_{\infty h}$ symmetry (Figure 4g-1,g-2). Upon further increase in $L$, the loop buckles either in-plane into an oval ($D_{2h}$ system symmetry in Figure 4h-1 to 4h-3) or out-of-plane into a shallow saddle ($C_{2v}$ symmetry in Figure 4i-1). The out-of-plane pathway is favored at lower $c_0R$ but is suppressed for stiff filaments, explaining its absence in Figure 4D. For the flexible filaments, further reduction in $c_0R$ stabilizes the stomatocyte geometry. Under this strongly concave confinement, the system undergoes a transition from $C_{2v}$ to $C_1$ symmetry, accompanied by pronounced out-of-plane deformation of the filament into highly distorted saddle-like shapes confined within the stomatocyte interior (Figure 4i-4).

For $c_0R < -0.3$, the filament-free vesicle adopts a stomatocyte shape. While short filaments remain circular (Figure 4c-1), the subsequent evolution becomes strongly stiffness-dependent. Flexible filaments ($D/(\kappa R) = 1$) undergo buckling within the confined interior, forming saddle-like configurations with $C_{2v}$ system symmetry for $c_0R > -1.15$ (Figure 4i-2), or $C_s$ symmetry for $c_0R < -1.15$ (Figure 4i-3). Further elongation leads to strong out-of-plane deformation and reorientation, ultimately resulting in complete symmetry breaking ($C_1$ symmetry in Figure 4i-4). In contrast, stiff filaments ($D/(\kappa R) = 10$) resist buckling and instead deform the vesicle, leading to expansion and flattening of the stomatocyte (Figure 4c-2) and eventually widening of the constricted neck (Figure 4c-3 and Figure S6B for 4c-4).

The underlying physical mechanisms are analyzed in detail in the SI Note 2. Figures S7 and S8 show that these transitions are governed by curvature-dependent redistribution of elastic energy between membrane reshaping and filament bending, with membrane tension providing complementary signatures of both continuous and discontinuous transitions.

We finally consider the rigid-filament limit, which isolates the geometric constraints imposed by vesicle confinement. In this limit, the filament remains strictly circular and is restricted to rigid-body translation and rotation. As a result, symmetry classes that rely on in-plane or out-of-plane filament bending, such as $D_{2h}$, $D_{2d}$, and $D_2$, are excluded (Figure 5). The accessible states are therefore limited to axisymmetric prolate, oblate, and stomatocyte shapes ($C_{\infty v}$), along with a small set of nonaxisymmetric states ($C_s$ and $C_{2h}$) arising from rigid-body rotation of the filament.

In contrast to flexible filaments, the rigid-filament limit introduces a strict upper bound on the admissible filament length, determined by the geometric capacity of the confining vesicle. For $v = 0.9$, the axisymmetric vesicle possesses a maximum equatorial radius $r_{max} = 1.211R$, essentially independent of $c_0R$. This sets an upper bound on the filament length $L_{max} = 2\pi r_{max} = 7.609R$ (Figure 5A). For $v = 0.65$, the vesicle has a larger $r_{max} = 1.334R$, leading to a correspondingly larger upper bound $L_{max} = 8.382R$ (Figure 5B). Further numerical results show that $r_{max}/R$ as a function of $v$ can be accurately approximated by the two-parameter expression $v = \{1 - [(r_{max}/R)^2 - 1]^a\}^b$, with fitted coefficients $a = 2.22$ and $b = 0.505$. Remarkably, the simpler expression

$$v = \sqrt{1 - \left[\left(\frac{r_{max}}{R}\right)^2 - 1\right]^{11/5}}$$

achieves nearly the same accuracy throughout the entire range $v \in [0, 1]$.

The inaccessible region reflects the finite accommodation capacity of a vesicle with prescribed area and volume. Beyond a critical filament-imposed span, no mechanically equilibrated configuration can satisfy the geometric and confinement constraints. Similar inaccessible regimes reported for vesicles


https://doi.org/10.1021/acs.nanolett.6c02160
Nano Lett. 2026, 26, 10273−10280

enclosing rigid straight rods[40] suggest that this limit is not specific to loop geometry.

A central outcome of this study is that filament−vesicle morphologies are jointly controlled by reduced volume, membrane spontaneous curvature, and filament deformability through their effects on confinement geometry and elastic-energy redistribution. Reduced volume sets the global anisotropy of confinement: larger $v$ favors weakly anisotropic, higher-symmetry states, whereas smaller $v$ creates a pronounced waist and partitions the vesicle into lobes. Stiff filament loops tend to remain within one lobe and expand it, while flexible loops can traverse the constricted neck, at the cost of both filament bending and deformation of highly curved membrane regions. Spontaneous curvature further biases these pathways by stabilizing compatible membrane shapes. This contrasts with nearly spherical vesicles, where isotropic confinement does not favor specific buckling directions and filament loops mainly retain higher-symmetry configurations.[26] The comparison with rigid filament limits highlights the role of deformability: elastic filaments adapt to anisotropic confinement and stabilize low-symmetry states, whereas rigid filaments are restricted by geometric bounds.

This mechanical picture provides a direct bridge to membrane-confined closed or quasi-closed cytoskeletal structures. Ring-like filament assemblies have been observed in reconstituted vesicle systems, where polymerizing actin can self-organize into equatorial rings and cross-linked actin can form stable bundles inside giant vesicles.[21,24] A close cellular example is the platelet marginal band, a peripheral microtubule ring that supports the discoid platelet shape and buckles into saddle-like configurations during activation as the cell rounds.[23,41] Because such loops lack free ends, they cannot relax confinement by end displacement and instead undergo global reorientation, in-plane narrowing, out-of-plane buckling, and symmetry breaking, consistent with the circular, oval, saddle-like, and figure-eight-like configurations predicted here.

The relevance also extends to membrane remodeling and synthetic-cell design. Dynamin and ESCRT-III remodel membranes through filament reorganization, neck constriction, and curvature-driven shape changes.[42] Beyond single-vesicle morphogenesis, flattened oblate or discotic vesicles can serve as geometrically compatible units for stacked or rouleaux-like assemblies,[43] reminiscent of layered Golgi cisternae used for compartmentalized processing.[44] Figure 4 shows that filament length, stiffness, and spontaneous curvature regulate transitions among oblate-like, stomatocyte-like, and asymmetric states, suggesting a passive route to program flattened, invaginated, or asymmetric vesicle geometries. Although the present model does not simulate division, recent lipid-nucleotide multilamellar protocells show that caveola formation, core−shell asymmetry, and shell reconfiguration can drive asymmetric splitting into morphologically distinct progeny,[45] further supporting the relevance of curvature- and confinement-mediated remodeling.

## ■ ASSOCIATED CONTENT

### Supporting Information

The Supporting Information is available free of charge at https://pubs.acs.org/doi/10.1021/acs.nanolett.6c02160.

MATLAB .fig files for representative filament−vesicle configurations (ZIP)

Details of the spherical-harmonic parametrization, constrained energy minimization, symmetry classification, and supplementary figures of representative configurations, phase diagrams, energy decomposition, and membrane tension (PDF)

## ■ AUTHOR INFORMATION


### Corresponding Author

**Xin Yi** − *School of Mechanics and Engineering Science, Peking University, Beijing 100871, China;* orcid.org/0000-0002-4726-5765; Email: xyi@pku.edu.cn

### Authors

**Yaxin Fang** − *School of Mechanics and Engineering Science, Peking University, Beijing 100871, China*

**Chengyao Zhang** − *School of Mechanics and Engineering Science, Peking University, Beijing 100871, China;* orcid.org/0009-0003-5733-0502

**Meng Wang** − *School of Mechanics and Engineering Science, Peking University, Beijing 100871, China;* orcid.org/0000-0003-0035-109X

**Chao Shi** − *School of Mechanics and Engineering Science, Peking University, Beijing 100871, China*

Complete contact information is available at: https://pubs.acs.org/10.1021/acs.nanolett.6c02160


### Notes

The authors declare no competing financial interest.

## ■ ACKNOWLEDGMENTS

This work was supported by the National Natural Science Foundation of China under grant 12272004. Computational resources supported by the High-performance Computing Platform of Peking University are acknowledged.

## ■ REFERENCES


(1) Seifert, U. Configurations of fluid membranes and vesicles. *Adv. Phys.* **1997**, *46*, 13−137.

(2) Seifert, U.; Berndl, K.; Lipowsky, R. Shape transformations of vesicles: Phase diagram for spontaneous-curvature and bilayer-coupling models. *Phys. Rev. A* **1991**, *44*, 1182−1202.

(3) Lipowsky, R. Spontaneous tubulation of membranes and vesicles reveals membrane tension generated by spontaneous curvature. *Faraday Discuss.* **2013**, *161*, 305−331.

(4) Hossein, A.; Deserno, M. Spontaneous curvature, differential stress, and bending modulus of asymmetric lipid membranes. *Biophys. J.* **2020**, *118*, 624−642.

(5) Bahrami, A. H.; Lipowsky, R.; Weikl, T. R. Tubulation and aggregation of spherical nanoparticles adsorbed on vesicles. *Phys. Rev. Lett.* **2012**, *109*, 188102.

(6) Agudo-Canalejo, J.; Lipowsky, R. Critical particle sizes for the engulfment of nanoparticles by membranes and vesicles with bilayer asymmetry. *ACS Nano* **2015**, *9*, 3704−3720.

(7) Bahrami, A. H.; Weikl, T. R. Curvature-mediated assembly of Janus nanoparticles on membrane vesicles. *Nano Lett.* **2018**, *18*, 1259−1263.

(8) Kostina, N. Y.; Rahimi, K.; Xiao, Q.; Haraszti, T.; Dedisch, S.; Spatz, J. P.; Schwaneberg, U.; Klein, M. L.; Percec, V.; Möller, M.; et al. Membrane-mimetic dendrimersomes engulf living bacteria via endocytosis. *Nano Lett.* **2019**, *19*, 5732−5738.

(9) Yu, Q.; Dasgupta, S.; Auth, T.; Gompper, G. Osmotic concentration-controlled particle uptake and wrapping-induced lysis of cells and vesicles. *Nano Lett.* **2020**, *20*, 1662−1668.

(10) Azadbakht, A.; Meadowcroft, B.; Varkevisser, T.; Šarić, A.; Kraft, D. J. Wrapping pathways of anisotropic dumbbell particles by giant unilamellar vesicles. *Nano Lett.* **2023**, *23*, 4267−4273.
(11) van der Ham, S.; Brown, A.; Kusumaatmaja, H.; Vutukuri, H. R. From shallow to full wrapping: Geometry and deformability dictate lipid vesicle internalization. *Nano Lett.* **2025**, *25*, 16451−16458.
(12) Wang, M.; Yi, X. Bulging-to-budding transition of lipid droplets confined within vesicle membranes. *Langmuir* **2021**, *37*, 12867−12873.
(13) Lim, H. W. G.; Wortis, M.; Mukhopadhyay, R. Stomatocyte-discocyte-echinocyte sequence of the human red blood cell: Evidence for the bilayer-couple hypothesis from membrane mechanics. *Proc. Natl. Acad. Sci. U.S.A.* **2002**, *99*, 16766−16769.
(14) Steinkühler, J.; Knorr, R. L.; Zhao, Z.; Bhatia, T.; Bartelt, S. M.; Wegner, S.; Dimova, R.; Lipowsky, R. Controlled division of cell-sized vesicles by low densities of membrane-bound proteins. *Nat. Commun.* **2020**, *11*, 905.
(15) Winnikoff, J. R.; Milshteyn, D.; Vargas-Urbano, S. J.; Pedraza-Joya, M. A.; Armando, A. M.; Quehenberger, O.; Sodt, A.; Gillilan, R. E.; Dennis, E. A.; Lyman, E.; et al. Homeocurvature adaptation of phospholipids to pressure in deep-sea invertebrates. *Science* **2024**, *384*, 1482−1488.
(16) Kattan, J.; Doerr, A.; Dogterom, M.; Danelon, C. Shaping liposomes by cell-free expressed bacterial microtubules. *ACS Synth. Biol.* **2021**, *10*, 2447−2455.
(17) Pogoda, K.; Byfield, F.; Deptuła, P.; Cieśluk, M.; Suprewicz, Ł.; Skłodowski, K.; Shivers, J. L.; van Oosten, A.; Cruz, K.; Tarasovetc, E.; et al. Unique role of vimentin networks in compression stiffening of cells and protection of nuclei from compressive stress. *Nano Lett.* **2022**, *22*, 4725−4732.
(18) Daly, M. L.; Nishi, K.; Klawa, S. J.; Hinton, K. Y.; Gao, Y.; Freeman, R. Designer peptide−DNA cytoskeletons regulate the function of synthetic cells. *Nat. Chem.* **2024**, *16*, 1229−1239.
(19) Graham, K.; Chandrasekaran, A.; Wang, L.; Yang, N.; Lafer, E. M.; Rangamani, P.; Stachowiak, J. C. Liquid-like condensates mediate competition between actin branching and bundling. *Proc. Natl. Acad. Sci. U.S.A.* **2024**, *121*, e2309152121.
(20) Negi, A.; Sakamoto, R.; Ienaga, R.; Miyazaki, M.; Maeda, Y. T. Myosin-driven advection and actin reorganization control the geometry of confined actomyosin gel. *Nano Lett.* **2025**, *25*, 17979−17987.
(21) Miyazaki, M.; Chiba, M.; Eguchi, H.; Ohki, T.; Ishiwata, S. Cell-sized spherical confinement induces the spontaneous formation of contractile actomyosin rings in vitro. *Nat. Cell Biol.* **2015**, *17*, 480−489.
(22) Tsai, F. C.; Koenderink, G. H. Shape control of lipid bilayer membranes by confined actin bundles. *Soft Matter* **2015**, *11*, 8834−8847.
(23) Dmitrieff, S.; Alsina, A.; Mathur, A.; Nédélec, F. J. Balance of microtubule stiffness and cortical tension determines the size of blood cells with marginal band across species. *Proc. Natl. Acad. Sci. U.S.A.* **2017**, *114*, 4418−4423.
(24) Litschel, T.; Kelley, C. F.; Holz, D.; Koudehi, M. A.; Vogel, S. K.; Burbaum, L.; Mizuno, N.; Vavylonis, D.; Schwille, P. Reconstitution of contractile actomyosin rings in vesicles. *Nat. Commun.* **2021**, *12*, 2254.
(25) Kohyama, S.; Merino-Salomón, A.; Schwille, P. In vitro assembly, positioning and contraction of a division ring in minimal cells. *Nat. Commun.* **2022**, *13*, 6098.
(26) Shi, C.; Zou, G.; Wu, Z.; Wang, M.; Zhang, X.; Gao, H.; Yi, X. Morphological transformations of vesicles with confined flexible filaments. *Proc. Natl. Acad. Sci. U.S.A.* **2023**, *120*, e2300380120.
(27) Sciortino, A.; Faizi, H. A.; Fedosov, D. A.; Frechette, L.; Vlahovska, P. M.; Gompper, G.; Bausch, A. R. Active membrane deformations of a minimal synthetic cell. *Nat. Phys.* **2025**, *21*, 799−807.
(28) Shi, C.; Zhang, C.; Fang, Y.; Yi, X. Flexible filaments in vesicles with reduced volume: Anisotropic confinement and morphological response. *J. Mech. Phys. Solids* **2026**, *206*, 106383.
(29) Behera, A.; Kumar, G.; Sain, A. Confined filaments in soft vesicles — the case of sickle red blood cells. *Soft Matter* **2020**, *16*, 421−427.
(30) Zhang, C.; Fang, Y.; Shi, C.; Yuan, H.; Yi, X. Stretching transition of vesicles with confined filament loops: Morphological evolution with filament distortion and reorientation. *Giant* **2024**, *17*, 100233.
(31) Zhang, C.; Zou, G.; Fang, Y.; Gao, H.; Yi, X. Interacting filaments drive vesicle morphogenesis. *Nat. Commun.* **2026**, *17*, 78.
(32) Vázquez-Montejo, P.; McDargh, Z.; Deserno, M.; Guven, J. Cylindrical confinement of semiflexible polymers. *Phys. Rev. E* **2015**, *91*, 063203.
(33) Wang, M.; Yi, X. Equilibrium analysis of surface-constrained elastic rods: Unveiling contact and internal forces through local geometry. *J. Mech. Phys. Solids* **2024**, *187*, 105635.
(34) Janzen, G.; Mackay, E. D.; Sknepnek, R.; Matoz-Fernandez, D. A. Active filaments on curved surfaces: From single filaments to dilute suspensions. *Soft Matter* **2026**, *22*, 474−484.
(35) Vázquez-Montejo, P.; Božič, B.; Guven, J. Equatorial deformation of homogeneous spherical fluid vesicles by a rigid ring. *Phys. Rev. E* **2025**, *111*, 035411.
(36) Helfrich, W. Elastic properties of lipid bilayers: Theory and possible experiments. *Z. Naturforsch. C* **1973**, *28*, 693−703.
(37) Doi, M.; Edwards, S. F. *The Theory of Polymer Dynamics*; Oxford University Press: Oxford, United Kingdom, 1986.
(38) Khairy, K.; Howard, J. Minimum-energy vesicle and cell shapes calculated using spherical harmonics parameterization. *Soft Matter* **2011**, *7*, 2138−2143.
(39) Nocedal, J.; Wright, S. J. *Numerical Optimization*, 2nd ed.; Springer: New York, 2006.
(40) Wu, Z.; Yuan, H.; Zhang, X.; Yi, X. Sidewall contact regulating the nanorod packing inside vesicles with relative volumes. *Soft Matter* **2019**, *15*, 2552−2559.
(41) Diagouraga, B.; Grichine, A.; Fertin, A.; Wang, J.; Khochbin, S.; Sadoul, K. Motor-driven marginal band coiling promotes cell shape change during platelet activation. *J. Cell Biol.* **2014**, *204*, 177−185.
(42) Meadowcroft, B.; Palaia, I.; Pfitzner, A.-K.; Roux, A.; Baum, B.; Šarić, A. Mechanochemical rules for shape-shifting filaments that remodel membranes. *Phys. Rev. Lett.* **2022**, *129*, 268101.
(43) Ziherl, P.; Svetina, S. Flat and sigmoidally curved contact zones in vesicle−vesicle adhesion. *Proc. Natl. Acad. Sci. U.S.A.* **2007**, *104*, 761−765.
(44) Huang, S.; Wang, Y. Golgi structure formation, function, and post-translational modifications in mammalian cells. *F1000Research* **2017**, *6*, 2050.
(45) Meng, H.; Jia, L.; Qiu, D.; Lin, Y.; Wang, S.; Mann, S.; Qiao, Y. Asymmetric splitting in dividing lipid-nucleotide multilamellar droplets. *Nature* **2026**, *653*, 418−424.


https://doi.org/10.1021/acs.nanolett.6c02160
*Nano Lett.* 2026, 26, 10273−10280

**Supporting Information for**

# Spontaneous curvature sculpts filament–vesicle morphogenesis

Yaxin Fang, Chengyao Zhang, Meng Wang, Chao Shi, Xin Yi*

School of Mechanics and Engineering Science, Peking University, Beijing, China

*E-mail: xyi@pku.edu.cn

**This PDF file includes**:

Supporting text

Figures S1 to S8

Tables S1 and S2

**Other Supporting Information files:**

MATLAB .fig files for representative filament–vesicle configurations

**Note 1. Representation of the filament–vesicle system and its energy minimization**

The vesicle surface is represented using a spherical harmonic parameterization. In a Cartesian coordinate system, the position vector $\mathbf{r}^{\mathrm{m}}$ of the vesicle surface is represented as (ref. 38)

$$\mathbf{r}^{\mathrm{m}}(\theta,\varphi)=\begin{bmatrix} x^{\mathrm{m}}(\theta,\varphi) \\ y^{\mathrm{m}}(\theta,\varphi) \\ z^{\mathrm{m}}(\theta,\varphi) \end{bmatrix}=\begin{bmatrix} \sum_{l=0}^{l_{\max}}\sum_{k=-l}^{l} C_{lk}^{x} Y_{lk}(\theta,\varphi) \\ \sum_{l=0}^{l_{\max}}\sum_{k=-l}^{l} C_{lk}^{y} Y_{lk}(\theta,\varphi) \\ \sum_{l=0}^{l_{\max}}\sum_{k=-l}^{l} C_{lk}^{z} Y_{lk}(\theta,\varphi) \end{bmatrix},$$

where $\theta\in[0,\pi]$ and $\varphi\in[0,2\pi]$ denote the polar and azimuthal angles in a spherical coordinate system, respectively (Figure 1), and $C_{lk}^{x,y,z}$ are control coefficients. In our calculations, the spherical harmonic expansions are truncated at $l = l_{\max}$. Since each Cartesian coordinate contains $(l_{\max} + 1)^2$ real spherical harmonic modes, the vesicle shape is described by $3(l_{\max} + 1)^2$ control coefficients. We use $l_{\max} = 5$ for prolate and oblate vesicle shapes and $l_{\max} = 7$ for stomatocyte shapes, for which additional modes are required to resolve the invaginated neck region. Convergence tests (not shown here) performed for representative nonspherical equilibrium states confirm that these truncation orders are sufficient to capture the equilibrium shapes and energy components reported in this work.

Here, $Y_{lk}(\theta,\varphi)$ is the real spherical harmonic function defined as

$$Y_{lk}(\theta,\varphi)=\begin{cases} \sqrt{2}N_{lk}P_{lk}(\cos\theta)\cos(k\varphi), & k>0, \\ N_{l0}P_{l0}(\cos\theta), & k=0, \\ \sqrt{2}N_{lk}P_{lk}(\cos\theta)\sin(-k\varphi), & k<0, \end{cases}$$

with

$$N_{lk}=\sqrt{\frac{(2l+1)(l-|k|)!}{4\pi(l+|k|)!}} \quad \text{and} \quad P_{lk}(x)=(-1)^{|k|}\frac{1-x^2}{2^l l!}\frac{\mathrm{d}^{l+|k|}[(x^2-1)^l]}{\mathrm{d}x^{l+|k|}}.$$

For the surface-constrained filament, the filament centerline is prescribed as a curve on the vesicle surface. Its position vector $\mathbf{r}^{\mathrm{f}}$ is written as $\mathbf{r}^{\mathrm{f}}(\varphi) = \mathbf{r}^{\mathrm{m}}(\theta_0,\varphi)$ with $\theta_0$ as a prescribed polar angle. Therefore, the filament is not independently parameterized; its geometry is determined by the same spherical harmonic coefficients $C_{lk}^{x,y,z}$ that define the vesicle surface. The geometrical quantities of both the vesicle surface and the filament, including surface curvatures and filament curvature, are computed from $\mathbf{r}^{\mathrm{m}}(\theta,\varphi)$ and $\mathbf{r}^{\mathrm{f}}(\varphi)$ using classical differential geometry.

For the vesicle surface represented by $\mathbf{r}^{\mathrm{m}}(\theta,\varphi)$, its local mean curvature $H$ is given by

$$H=\frac{EN-2FM+GL}{2(EG-F^2)},$$

where $E=\mathbf{r}_{,\theta}^{\mathrm{m}}\cdot\mathbf{r}_{,\theta}^{\mathrm{m}}$, $F=\mathbf{r}_{,\theta}^{\mathrm{m}}\cdot\mathbf{r}_{,\varphi}^{\mathrm{m}}$, $G=\mathbf{r}_{,\varphi}^{\mathrm{m}}\cdot\mathbf{r}_{,\varphi}^{\mathrm{m}}$, $L=\mathbf{r}_{,\theta\theta}^{\mathrm{m}}\cdot\mathbf{n}^{\mathrm{m}}$, $M=\mathbf{r}_{,\theta\varphi}^{\mathrm{m}}\cdot\mathbf{n}^{\mathrm{m}}$, and $N=\mathbf{r}_{,\varphi\varphi}^{\mathrm{m}}\cdot\mathbf{n}^{\mathrm{m}}$ are coefficients of the first and second fundamental forms of the surface at the point $\mathbf{r}^{\mathrm{m}}$, with $\mathbf{n}^{\mathrm{m}}=(\mathbf{r}_{,\theta}^{\mathrm{m}}\times\mathbf{r}_{,\varphi}^{\mathrm{m}})/|\mathbf{r}_{,\theta}^{\mathrm{m}}\times\mathbf{r}_{,\varphi}^{\mathrm{m}}|$ as the outward unit normal vector to the surface. $H$ is negative for a spherical vesicle. Henceforth, a subscript comma followed by a variable indicates partial differentiation with respect to that variable (e.g., $\mathbf{r}_{,\theta}^{\mathrm{m}}\equiv\partial\mathbf{r}^{\mathrm{m}}/\partial\theta$).

The area element of the vesicle surface is $\mathrm{d}A = |\mathbf{r}^{\mathrm{m}}_{,\theta} \times \mathbf{r}^{\mathrm{m}}_{,\varphi}|\,\mathrm{d}\theta\mathrm{d}\varphi = \sqrt{g}\,\mathrm{d}\theta\mathrm{d}\varphi$, and the surface area is $A = \int_0^{2\pi}\int_0^{\pi}\sqrt{g}\,\mathrm{d}\theta\mathrm{d}\varphi$.

The vesicle volume is $V = \frac{1}{3}\int_0^{2\pi}\int_0^{\pi}\mathbf{r}^{\mathrm{m}}\cdot(\mathbf{r}^{\mathrm{m}}_{,\theta}\times\mathbf{r}^{\mathrm{m}}_{,\varphi})\mathrm{d}\theta\mathrm{d}\varphi$.

The bending energy of the vesicle membrane is $E_{\mathrm{m}} = \frac{\kappa}{2}\int_0^{2\pi}\int_0^{\pi}(2H + c_0)^2\sqrt{g}\,\mathrm{d}\theta\mathrm{d}\varphi$.

For the filament represented by $\mathbf{r}^{\mathrm{f}}(\varphi)$, its local curvature is $C = \frac{|\mathbf{r}^{\mathrm{f}}_{,\varphi}\times\mathbf{r}^{\mathrm{f}}_{,\varphi\varphi}|}{|\mathbf{r}^{\mathrm{f}}_{,\varphi}|^3}$ and its bending energy is $E_{\mathrm{f}} = \frac{D}{2}\int_0^{2\pi}\frac{|\mathbf{r}^{\mathrm{f}}_{,\varphi}\times\mathbf{r}^{\mathrm{f}}_{,\varphi\varphi}|^2}{|\mathbf{r}^{\mathrm{f}}_{,\varphi}|^5}\mathrm{d}\varphi$.

The vesicle area $A$, the enclosed volume specified by the reduced volume $v$, and the filament length $L$ are imposed as equality constraints in the numerical minimization. The total elastic energy $E_{\mathrm{tot}}$, expressed as a function of the spherical harmonic control coefficients $C_{lk}^{x,y,z}$, is minimized using the MATLAB fmincon routine with the interior-point algorithm for constrained nonlinear optimization. The optimization variables are the spherical harmonic coefficients $C_{lk}^{x,y,z}$ defining the vesicle surface. Since the filament centerline is constrained to lie on the vesicle surface, its configuration is also determined by $C_{lk}^{x,y,z}$.

Using the interior-point method (ref. 39), both first- and second-order derivatives of the total energy and equality constraints with respect to $C_{lk}^{x,y,z}$ are supplied either explicitly or implicitly. The interior-point algorithm then iteratively solves the constrained minimization problem by satisfying the corresponding Karush–Kuhn–Tucker (KKT) optimality conditions. First-order derivatives (gradients) determine descent directions and KKT optimality criteria. Second-order derivatives (Hessian matrices) capture local curvature of objective functions. They enable quadratic convergence of Newton iterations, greatly accelerating the interior-point method. Quasi-Newton techniques approximate Hessian matrices using gradient data to reduce computational cost. Upon convergence, the optimized coefficients determine the equilibrium vesicle shape, filament configuration, and corresponding energy components.

For each prescribed set of model parameters, including $v$, $c_0R$, $L/R$, and $D/(\kappa R)$, multiple optimization trials are performed from different initial configurations. These include neighboring solutions obtained by continuation in parameter space, simple reference shapes, and symmetry-perturbed configurations. The converged stationary configurations are compared by their total elastic energies, and the lowest-energy configuration is selected as the equilibrium state for constructing the morphological phase diagrams. Discontinuous boundaries are identified from energy crossings between distinct low-energy solution families, whereas continuous transitions are determined from smooth variations in morphology, symmetry, total energy, and membrane tension.

## Note 2. Supplementary numerical results

### A. Symmetry classifications in Schönflies notation

In this work, equilibrium configurations of the filament–vesicle system are classified according to their symmetry elements using Schönflies notation (Table S1). The distinct symmetry point groups identified in the phase diagrams are defined based on the presence of rotation axes, reflection planes, and inversion centers.

**Table S1.** The Schönflies point groups used in this work.

| Point groups | Definitions |
|---|---|
| $C_{\infty v}$ | axisymmetric configurations with a principal axis of infinite-fold rotational symmetry and infinitely many vertical mirror planes, but without a horizontal mirror plane or inversion center |
| $D_{\infty h}$ | axisymmetric configurations with a principal axis of infinite-fold rotational symmetry, infinitely many vertical mirror planes, a horizontal mirror plane, and an inversion center |
| $C_s$ | configurations possessing a single mirror plane |
| $C_{2h}$ | configurations possessing a two-fold rotation axis, a horizontal mirror plane, and an inversion center |
| $D_{2d}$ | configurations with a four-fold improper rotation axis, two mutually perpendicular two-fold axes, and two vertical dihedral mirror planes |
| $D_2$ | configurations with three mutually perpendicular two-fold rotation axes and no mirror plane |
| $D_{2h}$ | configurations with three mutually perpendicular two-fold rotation axes, three mutually perpendicular mirror planes, and an inversion center |
| $C_{2v}$ | configurations with a two-fold rotation axis and two mutually perpendicular vertical mirror planes intersecting at the axis |
| $C_1$ | configurations with no symmetry other than the identity |

**B. Equilibrium morphologies of filament-free vesicles**

We characterize the equilibrium morphologies of filament-free vesicles as functions of the reduced volume $v$ and normalized spontaneous curvature $c_0R$ in Figure S1. At zero spontaneous curvature ($c_0 = 0$), the vesicle remains spherical at $v = 1$, and transitions through prolate ($v \in (0.651,1)$), oblate ($v \in (0.591,0.651)$), and stomatocyte ($v \in (0,0.591)$) morphologies as $v$ decreases.

When spontaneous curvature is introduced, the filament-free vesicle morphologies at given $v$ become sensitive to $c_0R$. For a filament-free vesicle of $v = 0.9$, the vesicle adopts a convex prolate shape when $c_0R > -0.984$ and a convex oblate shape when $c_0R < -0.984$ (Figure S1A). At $v = 0.65$, the filament-free vesicle exhibits three stable morphologies depending on the value of $c_0R$: a concave prolate (dumbbell) shape ($c_0R > 0.006$), a concave oblate (discocyte) shape ($-0.3 < c_0R \leq 0.006$), and a stomatocyte ($c_0R \leq -0.3$) (Figure S1B).

All these vesicle morphologies are axisymmetric (Figure S1). The prolate and oblate branches belong to the $D_{\infty h}$ point group, whereas the stomatocyte shape is classified as $C_{\infty v}$ group (Table S1).

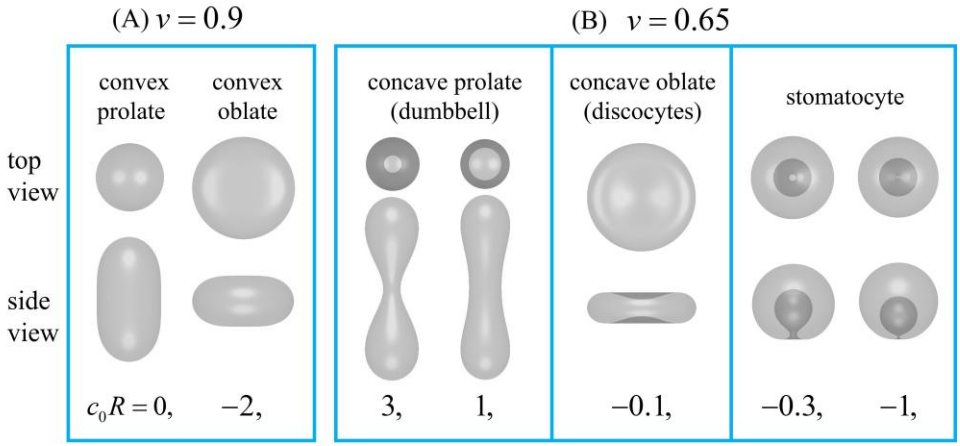


**Figure S1. Selected axisymmetric vesicle morphologies at reduced volumes $v$ = 0.9 (A) and 0.65 (B).** Corresponding values of $c_0R$ are indicated below each morphology. Our morphological predictions, obtained via spherical harmonic parameterization and numerical optimization, agree well with the axisymmetric solutions reported in ref. 2, which are derived by solving the Euler–Lagrange equations.

These filament-free equilibrium states define the soft-confinement geometries. In particular, the contrast between $v$ = 0.9 and $v$ = 0.65 is central to the morphology selection of the coupled filament–vesicle system: the former provides convex confinement and primarily probes filament-induced symmetry breaking, whereas the latter introduces lobe-selective and neck-mediated confinement, enabling qualitatively new transition pathways and lower-symmetry configurations.

### C. Morphological phase diagrams and profiles of energy and membrane-tension at different reduced volumes

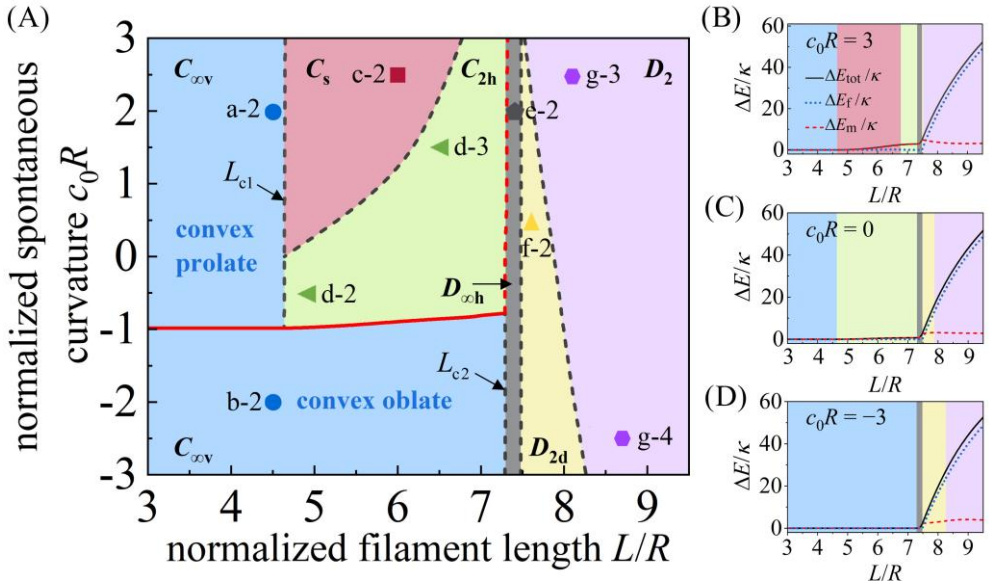


**Figure S2. Morphological transitions and energy decomposition profiles at $v$ = 0.9 and $D/(\kappa R)$ = 10.** (A) Morphological phase diagram of the filament–vesicle system in $L/R$–$c_0R$ space. Symbols correspond to the morphologies shown in Figure 2 in the main text. (B–D) Profiles of the total elastic energy change $\Delta E_{tot}$ and its components $\Delta E_f$ and $\Delta E_m$ at $c_0R$ = 3, 0, and −3, respectively. Dashed (solid) phase boundaries indicate continuous (discontinuous) morphological transitions.

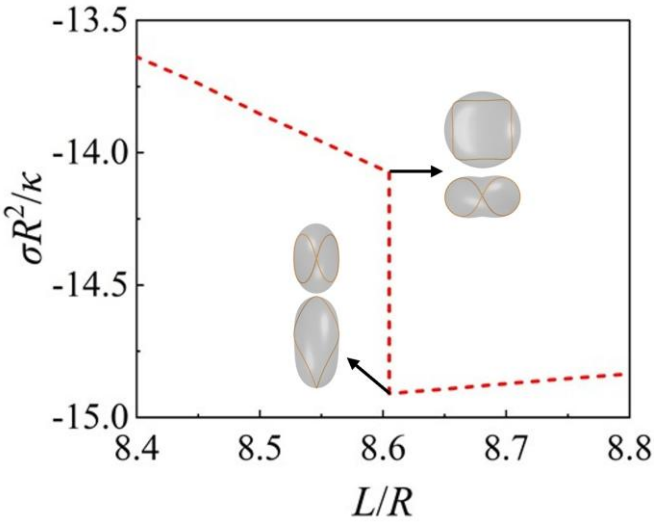


**Figure S3. Enlarged view of the abrupt drop in the normalized membrane tension $\sigma R^2/\kappa$ at $v = 0.9$, $D/(\kappa R) = 1$, and $c_0R = -3$, corresponding to the dotted red curve in Figure 3E.** The two sets of configurations shown at $L/R = 8.605$ illustrate the transition from an oblate vesicle with a saddle-like filament to a prolate vesicle with a figure-eight-like filament. In each set, the upper image shows the top view and the lower image shows the side view.

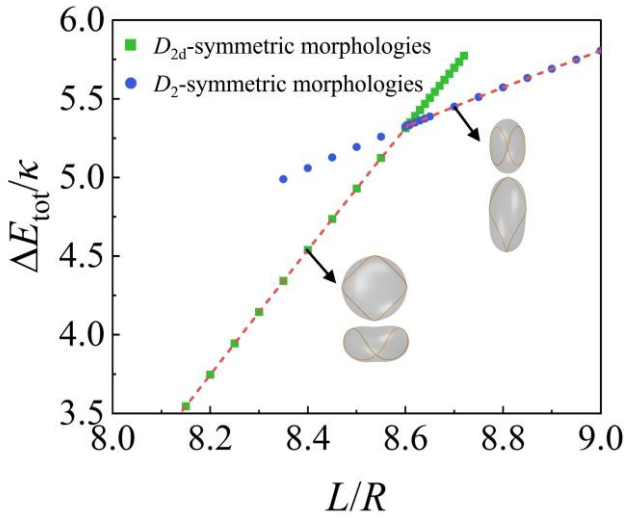


**Figure S4. Total energy changes of the two locally stable morphological families across the $D_{2d}$-to-$D_2$ discontinuous transition boundary in Figure 3A at $v = 0.9$, $D/(\kappa R) = 1$, and $c_0R = -3$.** Green squares denote the $D_{2d}$-symmetric morphologies, and blue circles denote the $D_2$-symmetric morphologies. The dashed red segments represent the lower-energy envelope selected as the equilibrium energy. The energy crossing occurs at $L/R = 8.605$, where the equilibrium state switches discontinuously from the $D_{2d}$-symmetric morphology to the $D_2$-symmetric morphology. In each configuration set, the upper image shows the top view and the lower image shows the side view.

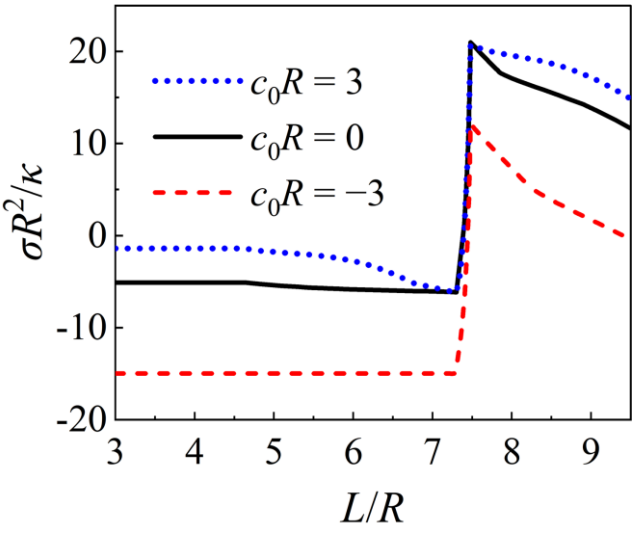


**Figure S5. Profiles of the normalized membrane tension $\sigma R^2/\kappa$ at $v = 0.9$ and $D/(\kappa R) = 10$ for $c_0R = -3$, 0, and 3.** The morphological transitions here are continuous.

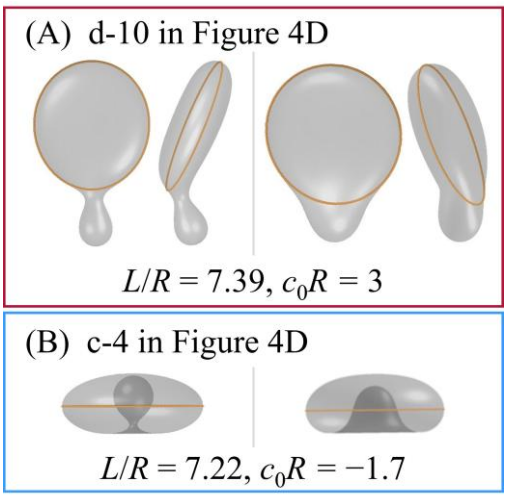


**Figure S6. Selected system configurations at $v = 0.65$ and $D/(\kappa R) = 10$.** (A) $c_0R = 3$, $L/R = 7.39$; (B) $c_0R = -1.7$, $L/R = 7.22$. In each panel, the left and right images show two coexisting configurations at the same parameter values.

For the vesicles with reduced volume $v = 0.65$, stiff filaments of $D/(\kappa R) = 10$ undergo negligible deformation, and the vesicle correspondingly conforms to the circular filament geometry. At $c_0R = 3$ and $L/R = 7.39$ (d-10 configurations in Figure 4D), two system configurations coexist: one retaining a narrow waist (left) and the other exhibiting a widened waist (right). The narrow-waist configuration becomes energetically unfavorable as $L$ increases. Similarly, at $c_0R = -1.7$ and $L/R = 7.22$ (c-4 configurations in Figure 4D), stomatocyte vesicles display two different invaginated configurations: one with a narrow-necked invagination (left) and the other with a broad invagination without a pronounced neck (right). With increasing $L$, the latter configuration is energetically favored.

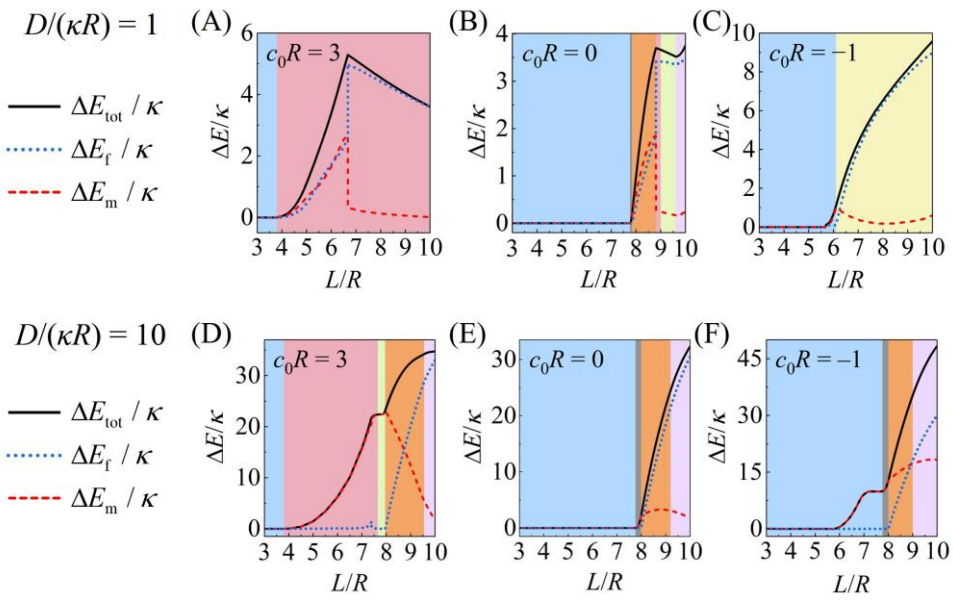


**Figure S7. Profiles of the total elastic energy change $\Delta E_{tot}$ and its components $\Delta E_f$ and $\Delta E_m$ at $v = 0.65$.** Panels (A–C) correspond to $D/(\kappa R) = 1$ and panels (D–F) to $D/(\kappa R) = 10$.

Complementing the phase diagrams at $v = 0.65$, Figure S7 presents the total energy change $\Delta E_{tot}$ along with its membrane and filament contributions, $\Delta E_m$ and $\Delta E_f$, for flexible ($D/(\kappa R) = 1$) and stiff ($D/(\kappa R) = 10$) filaments. The reference membrane energy $E_{m0}$ is $1.41\kappa$, $45.90\kappa$, and $68.38\kappa$ at $c_0R = 3$, 0, and −1, respectively. For flexible filaments (Figure S7A–C), at intermediate filament lengths, $\Delta E_m$ and $\Delta E_f$ contribute comparably for $c_0R = 3$ and 0, whereas $\Delta E_m$ dominates at $c_0R = -1$; at large $L$, $\Delta E_f$ dominates in all cases. For stiff filaments (Figure S7D–F), $\Delta E_m$ dominates at short and intermediate $L$ for $c_0R = 3$, whereas $\Delta E_f$ prevails at large $L$; at $c_0R = 0$, $\Delta E_f$ dominates throughout, and at $c_0R = -1$, $\Delta E_m$ governs the intermediate-$L$ regime while both $\Delta E_m$ and $\Delta E_f$ remain important at large $L$.

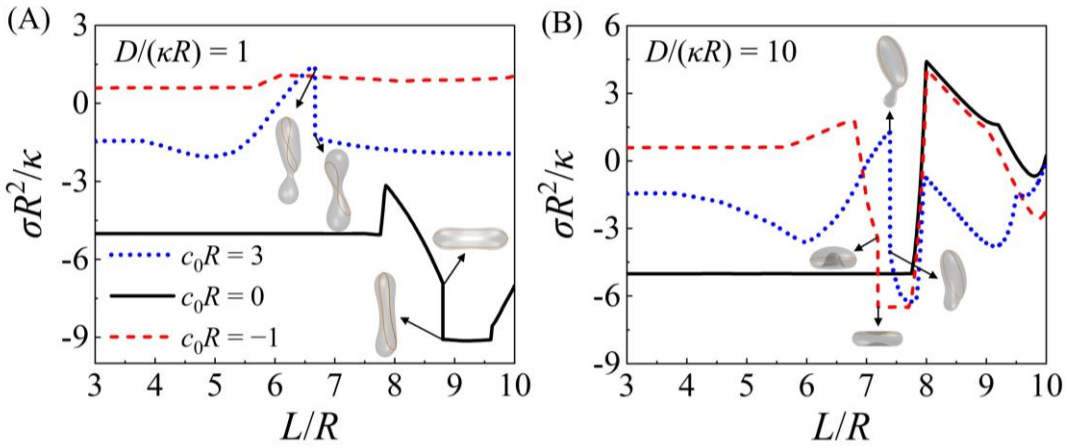


**Figure S8. Profiles of the normalized membrane tension $\sigma R^2/\kappa$ at $v = 0.65$ for filaments with $D/(\kappa R) = 1$ (A) and 10 (B).** In each panel, curves are shown for $c_0R = -1$, 0, and 3. Insets show representative transition configurations.

Figure S8 provides the membrane tension evolution as a function of filament length. For flexible filaments ($D/(\kappa R) = 1$), an abrupt drop in $\sigma$ at $c_0R = 3$ (dotted blue line) indicates a discontinuous transition in which the filament escapes single-lobe confinement to span the vesicle waist. At $c_0R = 0$, $\sigma$ first exhibits a sharp increase associated with a continuous $C_{\infty v}$-to-$D_{\infty h}$ transition, followed by a sudden decrease due to the discontinuous $D_{2h}$-to-$C_s$ transition. At $c_0R = -1$, the filament primarily accommodates stomatocyte confinement through bending, resulting in only weak tension variations.

For stiff filaments ($D/(\kappa R) = 10$), the tension variations are more pronounced. At $c_0R = 0$, $\sigma$ rises sharply during the continuous $C_{\infty v}$-to-$D_{\infty h}$ transition. At $c_0R = 3$ and $-1$, abrupt drops in $\sigma$ indicate discontinuous transitions that relieve membrane tension, corresponding to waist opening and the stomatocyte-to-oblate transformation, respectively. The subsequent tension evolution converges to a common continuous trajectory characterized by the $D_{2h}$-to-$D_2$ transition, regardless of $c_0R$.

**Note 3. Shared configuration data**

The MATLAB .fig files provided as Supporting Data contain representative optimized filament–vesicle configurations for visualization and inspection. Each file can be opened in MATLAB and rotated freely to examine the corresponding vesicle surface and filament-loop geometry. The plotted objects can also be used to extract representative geometric information from the displayed configurations.

The files are named using the format v[value]_NormL[value]_c0R[value]_SR[value].fig, where $v$ is the reduced volume, NormL denotes the normalized filament length $L/R$, c0R denotes the normalized spontaneous curvature $c_0R$, and SR denotes the stiffness ratio $D/(\kappa R)$. The corresponding parameter values are summarized in Table S2.

**Table S2.** MATLAB .fig files and corresponding model parameters.

| Shared .fig file | $v$ | $L/R$ | $c_0R$ | $D/(\kappa R)$ |
|---|---|---|---|---|
| v0.9_NormL4.5_c0R1_SR1.fig | 0.9 | 4.5 | 1 | 1 |
| v0.9_NormL5.6_c0R2.5_SR10.fig | 0.9 | 5.6 | 2.5 | 10 |
| v0.9_NormL7.475_c0R-2_SR10.fig | 0.9 | 7.475 | −2 | 10 |
| v0.9_NormL9_c0R2.4_SR1.fig | 0.9 | 9 | 2.4 | 1 |
| v0.65_NormL3.4_c0R2_SR1.fig | 0.65 | 3.4 | 2 | 1 |
| v0.65_NormL5.6_c0R-0.8_SR1.fig | 0.65 | 5.6 | −0.8 | 1 |
| v0.65_NormL7.1_c0R-1_SR10.fig | 0.65 | 7.1 | −1 | 10 |
| v0.65_NormL7_c0R1.5_SR10.fig | 0.65 | 7 | 1.5 | 10 |
| v0.65_NormL8_c0R-0.5_SR1.fig | 0.65 | 8 | −0.5 | 1 |
| v0.65_NormL9.2_c0R3_SR1.fig | 0.65 | 9.2 | 3 | 1 |